IEEE Access
Multidisciplinary | Rapid Review | Open Access Journal

Received 16 November 2023, accepted 18 December 2023, date of publication 25 December 2023,
date of current version 22 January 2024.

Digital Object Identifier 10.1109/ACCESS.2023.3346385

RESEARCH ARTICLE

Multi-Structure Parameter Optimization Analysis of Soft Actuator Based on Numerical Calculation

WANG SONGTAO[1,2,3], (Member, IEEE), YU YIMENG[1], JIANG SHIYU[1,3], AND CHEN SISI[1]
[1]School of Mechanical Engineering, Nanchang Institute of Technology, Nanchang 330099, China
[2]Research Institute of Tsinghua University in Shenzhen, Shenzhen 518057, China
[3]Key Laboratory of Precision Driving and Control of Jiangxi Province, Nanchang 330099, China

Corresponding author: Jiang Shiyu (shiyu_jiang@126.com)

This work was supported in part by the National Natural Science Foundation, China, under Grant 52265002; in part by the Jiangxi Natural Science Foundation under Grant 20232BAB204042; and in part by the Teaching Reform Program of Jiangxi Colleges and Universities under Grant JXJG22186.

ABSTRACT To optimize the performance of the soft actuator, numerical simulation and regression analysis of the multi-structure parameter are presented based on the numerical calculation method. Firstly, numerical simulation and regression analysis were performed on the parameters of different driving channel shapes, including equilateral triangle, square, regular pentagon, regular hexagon, and circle, to determine the driving performance under different channel cross-sections. Secondly, numerical simulation and regression analysis were conducted on the parameters of fiber winding diameter and winding angle of the soft actuator, and qualitative analysis was performed on the failure states of the numerical calculations. Lastly, numerical simulation and regression analysis were carried out on the parameters of wall thickness and driving channel length of the soft actuator to determine the influence of these parameters on the driving performance. Through the numerical simulation and regression analysis, this study provides a necessary theoretical foundation for the optimization design of soft actuator, effectively improving the development efficiency and dynamic performance of soft actuators.

INDEX TERMS Numerical calculation, parameter optimization, regression analysis, soft actuator.

I. INTRODUCTION

With the increasing demands of modern society for the flexibility, safety, and intelligence of robots, the robot industry and related sectors have been rapidly developing. As traditional rigid robots suffer from safety risks, poor environmental adaptability, and low flexibility, soft robots have been derived [1]. Soft robots, characterized by low stiffness, lightweight, infinite degrees of freedom, and the ability to withstand high-energy impacts, possess many superior comprehensive performance features, such as good safety, high flexibility, and applicability in various scenarios [2]. So far, soft robots have become a research hotspot in the field of robotics and have been widely applied in areas such as biomimetic robots [3], [4], [5], [6], [7], [8], healthcare [9], [10], and industry [11], [12], [13], [14], among other [15], [16], [17], [18], [19], [20].

In recent years, scholars both domestically and internationally have conducted extensive research on various soft robots. For example, Takanish Atsuo and Yuanzhong Li designed a flexible actuator (FMA) coupled with a fiber-software channel that can be used to mimic mouse bones. The FMA contains three chambers and one-third circle in each chamber, and the performance of FMA was examined, tested, and optimized [6]. Quansheng Jiang designed a pneumatic soft manipulator with a three-claw gripper and a clamp. The three claw gripper with a concave-shaped soft channel are spaced 120°apart. The relationship between the bending angle and pressure of the pneumatic manipulator is verified by experiments [12]. Jinrong Li designed an actuator that couples a compression spring with dielectric elastomers with a circular channel cross-section. The structural parameters of the actuator were optimized, and the effects of some design parameters on the performance of the actuator were analyzed and discussed. A thermodynamic model was established for predicting the deformation of actuator [20]. Elangona Tarajan

The associate editor coordinating the review of this manuscript and approving it for publication was Wai-Keung Fung.

designed an actuator with a concave-shaped soft channel and analyzed and optimized parameters such as the height of the cavity, wall thickness, number of cavities, and spacing between cavities. Subsequently, the actuator's good bending and stretching characteristics were experimentally validated [21]. Wenbiao Wang designed the US2A actuator, which has a circular cross-section of silicone tubing wrapped in a corrugated braided sleeve. A pressure-elongation and pressure-force model was established to reflect the influence of shell thickness and material of the silicone tubing on the performance of the actuator. Subsequently, the US2A actuator was optimized for various working conditions, and based on this, pneumatic rehabilitation gloves, soft arm robots, and rigid-soft coupled continuum robots were designed to further validate the feasibility of the US2A as a component of soft actuators [22]. Mingcan Li designed a corrugated tube actuator with a circular channel cross-section. Based on this, a novel simulation model was developed to simulate the elongation and anchoring motion of earthworms. The research results showed good agreement between experimental and simulated results [23]. Emilya Allen and Johnp Swensen designed a soft coupled actuator with a shape memory alloy (SMA) spring and a circular channel cross-section. The SMA spring was embedded in the wall of the actuator's soft channel. They used a pneumatic SMA (PneuSMA) actuator to achieve precise control of the actuator under different pressure and SMA conditions. They also established a finite element model to predict the deformation of the actuator under different pressure and SMA conditions [24]. Takahiro Kann designed an actuator coupled with a rubber cylinder and a soft channel. The rubber cylinder, made of springs or fibers, allowed the actuator to elongate axially and suppress excessive radial expansion. The relationship between pressure and elongation rate of the soft actuator was experimentally verified [25].

In summary, the current soft actuators mainly have circular and concave-shaped soft channels, and there is a lack of research on the influence of soft channel shapes and the winding fibers on the performance of the actuators. Therefore, this paper focuses on the numerical experiments and regression analysis of structural parameters such as the shape of the driving channel, diameter of the winding fibers, winding pitch, wall thickness, and length of the driving channel to explore the influence of multiple structural parameters on the performance of the actuators.

This paper is organized as follows: In the secondly section, numerical modeling and analysis are conducted to propose design solutions. Finite element models are established using Abaqus to analyze the parameters of the soft actuators and verify the feasibility of the design. In the thirdly section, the finite element simulation results of various soft actuator channel shapes and winding angle parameters are compiled, and a regression model is developed to examine the impact of these factors on performance. In the fourthly section, finite element simulation results of different winding fiber diameters, wall thicknesses, and driving channel lengths are summarized, and the regression models are established to analyze their influence on the performance of the actuators. In the finally section, the influence of multiple structural parameters on the performance of the actuators is summarized, and future directions of work are proposed.

II. MODELING PROCESS

A. NUMERICAL MODELING ANALYSIS

A variety of strain energy density equations can be used to describe the mechanical properties of rubber materials, which are typically thought of as incompressible and isotropic super elastomers. The Green approach is typically used to establish the strain energy density equation. The second kind of Piola-Kirchhoff stress K and strain energy density W (strain energy of unit volume) have the following relationship [33].

$$K = 2\frac{\partial W}{\partial C} \tag{1}$$

where C represents the Cauchy-Green deformation tensor, $K = F^{\mathrm{T}} \cdot F$, F represents the deformation gradient.

Under isothermal conditions, three invariants of the C can be used to explain the strain energy density equation of isotropic hyperelastic materials.

$$W = W(\mathrm{I}_C, \mathrm{II}_C, \mathrm{III}_C) \tag{2}$$

where

$$\begin{cases} \mathrm{I}_C = \mathrm{tr}C = \lambda_1^2 + \lambda_2^2 + \lambda_3^2 \\ \mathrm{II}_C = \dfrac{1}{2}[(\mathrm{tr}C)^2 - \mathrm{tr}C^2] = \lambda_1^2\lambda_2^2 + \lambda_2^2\lambda_3^2 + \lambda_3^2\lambda_1^2 \\ \mathrm{III}_C = \det C = \lambda_1^2\lambda_2^2\lambda_3^2 \end{cases} \tag{3}$$

where λ_1, λ_2 and λ_3 are three directions of stretch ratio respectively.

To obtain the derivative of the compound function, the following equation can be obtained according to Eq.1, Eq.2 and Eq.3.

$$K = 2\left[\left(\frac{\partial W}{\partial \mathrm{I}_C} + \mathrm{I}_C\frac{\partial W}{\partial \mathrm{II}_C}\right)\mathrm{I} - \frac{\partial W}{\partial \mathrm{II}_C}C + \mathrm{III}_C\frac{\partial W}{\partial \mathrm{III}_C}C^{-1}\right] \tag{4}$$

Eq.4 represents the stress-strain relationship of the hyperelastic body as described by the deformation tensor C and the right stress K.

According to $K = JF^{-1} \cdot \sigma \cdot \left(F^{-1}\right)^T$, $C = F^T \cdot F$, $B = F \cdot F^T$, $\mathrm{I}_B = \mathrm{I}_C$, $\mathrm{II}_B = \mathrm{II}_C$, $\mathrm{III}_B = \mathrm{III}_C$, $J = (\mathrm{III}_B)^{1/2}$, and Cayley-Hamilton theorem, Eq.4 can be transformed.

$$\sigma = 2\frac{1}{(\mathrm{III}_C)^{1/2}}\left[\left(\mathrm{II}_B\frac{\partial W}{\partial \mathrm{II}_B} + \mathrm{III}_B\frac{\partial W}{\partial \mathrm{III}_B}\right)I + \frac{\partial W}{\partial \mathrm{I}_B}B - \mathrm{III}_B\frac{\partial W}{\partial \mathrm{II}_B}B^{-1}\right] \tag{5}$$

Eq.5 represents the stress-strain relationship of the hyperelastic body as described by the left tensor B and the stress tensor.

According to $\mathrm{III}_B = \mathrm{III}_C = 1$, Eq.5 can be transformed.

$$\sigma = -pI + 2\frac{\partial W}{\partial \mathrm{I}_B}B - 2\frac{\partial W}{\partial \mathrm{II}_B}B^{-1} \tag{6}$$

where p is the hydrostatic pressure.

The σ, B and B^{-1} of isotropic materials having the same shaft, the primary stress in the principal axis system can be obtained.

$$\sigma_i = -p + 2\frac{\partial W}{\partial \mathrm{I}_B}\lambda_i^2 - 2\frac{\partial W}{\partial \mathrm{II}_B}\frac{1}{\lambda_i^2} \tag{7}$$

To move the indeterminate hydrostatic pressure term, the following equation can be obtained.

$$\sigma_i - \sigma_j = 2\frac{\partial W}{\partial \mathrm{I}_B}\left(\lambda_i^2 - \lambda_j^2\right) - 2\frac{\partial W}{\partial \mathrm{II}_B}\left(\frac{1}{\lambda_i^2} - \frac{1}{\lambda_j^2}\right) \tag{8}$$

The strain energy density function is described by the Rivlin model as the polynomial model, and the C_{00} is a constant of the material.

$$W = \sum_{i,j=0}^{\infty} C_{ij}(\mathrm{I}_C - 3)^i(\mathrm{II}_C - 3)^j, C_{00} = 0 \tag{9}$$

Although higher-order polynomial models can replicate the stress-strain relationship of hyperelastic materials, some constants are often difficult to determine. It can be difficult to obtain efficient higher order constants, particularly when there is a lack of experimental data.

By retaining the first term in Eq. 9, the Neo-Hookean model [26], [27] can be obtained.

$$W_{NH} = C_{10}\left(\mathrm{I}_C - 3\right) \tag{10}$$

By retaining the first two terms of Eq. 9 are retained, the Mooney-Rivlin model [28], [29], [30], [31], [32], [33], [34], [35], [36] can be obtained.

$$W_{MR} = C_{10}\left(\mathrm{I}_C - 3\right) + C_{01}\left(\mathrm{II}_C - 3\right) \tag{11}$$

Since a small number of terms are maintained, Neo-Hookean and Mooney-Rivlin models cannot effectively depict the stress-strain relationship and the inverse ““‘S’”” shape stress-strain curve under significant deformation, so it only useful in low strain conditions.

Yeoh preserves the term less than or equal to the third order and abandoning the IIC term in Eq. 9, the following equation can be obtained [29], [30], [31].

$$W_{Yeoh} = C_{10}\left(\mathrm{I}_C - 3\right) + C_{20}\left(\mathrm{I}_C - 3\right)^2 + C_{30}\left(\mathrm{I}_C - 3\right)^3 \tag{12}$$

The Yeoh model has the advantage of reflecting the inverse ““‘S’”” shape stress-strain curve under various deformation modes, but exhibits a ““‘soft’”” phenomena when predicting the stress-strain relationship of equiaxial tensile tests. The conventional binomial parameter form of the Yeoh model can accurately suit its stress-strain characteristics for the numerical experiments in this work [37], [38], [39].

$$W_{Yeoh} = C_{10}\left(\mathrm{I}_C - 3\right) + C_{20}\left(\mathrm{I}_C - 3\right)^2 \tag{13}$$

To achieve precise material properties, an elastic sample used to make the actuator is tested at 500 mm/min in accordance with ASTM D638 (Type IV) [35]. According to numerical experiments on the nonlinear behavior of Elastosil M4601 silicone material, the C10=0.11Mpa and C20=0.02Mpa of are obtained [36], [37].

B. NUMERICAL EXPERIMENTAL PROCEDURE

The finite element model of the actuator is established in Abaqus/Standard, which is a finite element analysis software based on implicit solution. Firstly, a three-dimensional solid model with specific winding angles is created in Solidworks and saved in x.t format. The angle is between the winding fiber and the bottom surface of elastic base. Then importing the file into Abaqus and creating the section, type of the elastic base and the winding fibers were homogeneous solid. According to [38] and [39], the silicone rubber used in the elastic matrix is the hyperelastic material, the fiber winding line is the elastic material. In the second-order Yeo model of ElastosilM4601, C1= C10=0.11Mpa and C2= C20=0.02Mpa. The Young's modulus of Kavla fiber line is 6500Mpa, and the Poisson's ratio is 0.2. The elastic base and the winding fibers are assembled together firstly, then large deformation is clicked and the step size and total number of steps are set. Next, the constraint relationship is defined, with the constraints between the elastic base and the winding fibers defined as tie connections. The tie connection is a constraint definition in Abaqus. Subsequently one end of the actuator is fixed. Finally, meshes are generated with consistent density. The elastic matrix is divided into C3D20H which is a mesh element type in Abaqus. The fiber winding line is divided into B32 which is a mesh element type in Abaqus. Gravity and friction effects are ignored. The entire cavity of the actuator was subjected to pressure simulation to mimic the inflated air pressure, with a pressure P applied uniformly, the standard atmospheric pressure Pa is taken as the relative zero pressure point (Pa=101.325Kpa). In the finite element model, a uniform pressure of 60 kPa is applied, and the initial length of the actuator is 100 mm, the initial radius is 6.5 mm, actuator wall thickness is 5 mm, and the diameter of the winding fibers is 0.5 mm. Numerical simulation are carried out to obtain experimental data.

$$\begin{cases} S_{Triangle} = \dfrac{\sqrt{3}}{4}a^2 \\ S_{Quadrilateral} = a^2 \\ S_{Pentagon} = 1.72a^2 \\ S_{Hexagon} = \dfrac{3\sqrt{3}}{2}a^2 \\ S_{Circle} = \pi r^2 \end{cases} \tag{14}$$

where $S_{Triangle}$ is the area of the triangle, $S_{Quadrilateral}$ is the area of the quadrilateral, $S_{Pentagon}$ is the area of the pentagon, $S_{Hexagon}$ is the area of the hexagon, S_{Circle} is the area of the circle, a is the length of the side, and r is the radius of the circle. The wall thickness is the thinnest point in the section

diagram. To eliminate the influence of the inflated area and ensure the same inflated area of 132.665cm^2, the number of windings turns corresponding to different winding angles and channel shapes was calculated according to Eq.14.

III. NUMERICAL ANALYSIS OF WINDING ANGLE AND CHANNEL SHAPE

According to the numerical simulation in Section II, the pressure is 60Kpa, the initial length of the actuator is 100mm, the initial radius is 6.5mm, the actuator wall thickness is 5mm and the winding fiber diameter is 0.5mm. The variation of elongation at 3°, 6°, 9°, 12° and 15° is analyzed. Numerical simulation are carried out and the results are analyzed.

A. EQUILATERAL TRIANGLE CHANNEL

The finite element analysis and regression analysis of the equilateral triangle channel actuator are shown in Fig. 1(a)-(c). Including the regression analysis of the elongation under different angles, the simulation results with Abaqus and the sectional drawing of equilateral triangle. The elongation values obtained from simulations and the time required for Abaqus simulations for the equilateral triangle channel actuator under specific winding angles are shown in Tab. 1.

TABLE 1. Elongation of equilateral triangle channel actuator.

Angle of winding	3°	6°	9°	12°	15°
Elongation/mm	4.04	3.36	5.45	3.41	3.41
Time/s	237	56	88	62	84

The regression analysis, elongation, simulation results, and simulation time for the equilateral triangle channel actuator are shown in Fig. 1(a)-(b) and Tab. 1. As the winding angle increases from 3° to 5°, the elongation decreases. Qualitative analysis suggests that as the constraint of the winding fibers on the soft channel decreases, the circumferential expansion increases, leading to a reduction in axial elongation characteristics. When the winding angle increases from 5° to 9.6°, the elongation increases. Qualitative analysis suggests that as the constraint of the winding fibers on the soft channel decreases, the effect of axial elongation becomes more significant than circumferential expansion, resulting in an increase in axial elongation characteristics. When the winding angle increases from 9.6° to 13.8°, the elongation decreases. Qualitative analysis suggests that as the constraint of the winding fibers on the soft channel decreases, the effect of circumferential expansion becomes more significant than axial elongation, leading to a reduction in axial elongation characteristics. When the winding angle increases from 13.8° to 15°, the elongation increases. Qualitative analysis suggests that due to insufficient constraint of the winding fibers on the soft channel, the effect of circumferential expansion becomes more significant than axial elongation, resulting in poor axial elongation characteristics. The maximum elongation value of 5.54 mm is achieved at a winding angle of approximately

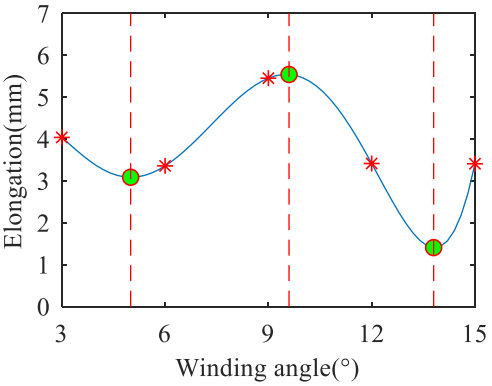

(a) Elongation

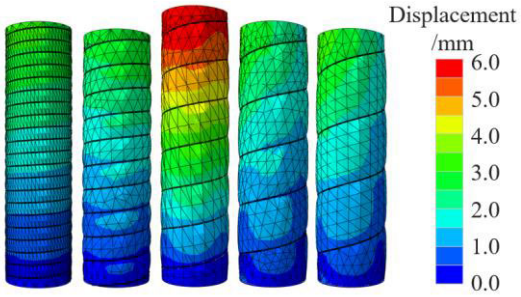

(b) Simulation diagram

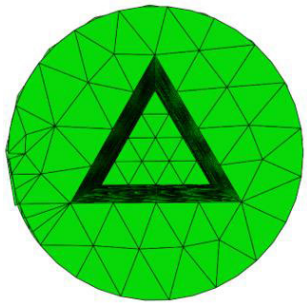

(c)© Sectional drawing

FIGURE 1. Equilateral triangle actuator.

9.6°. Therefore, when the actuator channel shape is an equilateral triangle, a winding angle of around 9.6° is optimal.

B. SQUARE CHANNEL

The finite element analysis and regression analysis of the regular square channel actuator are shown in Fig. 2(a)-(c). Including regression analysis of the elongation under different winding angles, the simulation results with Abaqus and the sectional drawing of square. The elongation values obtained from simulations and the time required for Abaqus simulations for the square channel actuator under specific winding angles are shown in Tab. 2.

The regression analysis, elongation, simulation results, and simulation time for square channel actuator are shown in Fig. 2(a)-(b) and Tab. 2. As the winding angle increases from 3° to 5°, the elongation decreases. Qualitative analysis suggests that as the constraint of the winding fibers on the soft channel decreases, the circumferential expansion increases,

TABLE 2. Elongation of square channel actuator.

Angle of winding	3°	6°	9°	12°	15°
Elongation/mm	4.56	3.95	5.65	3.46	3.03
Time/s	1136	116	56	34	80

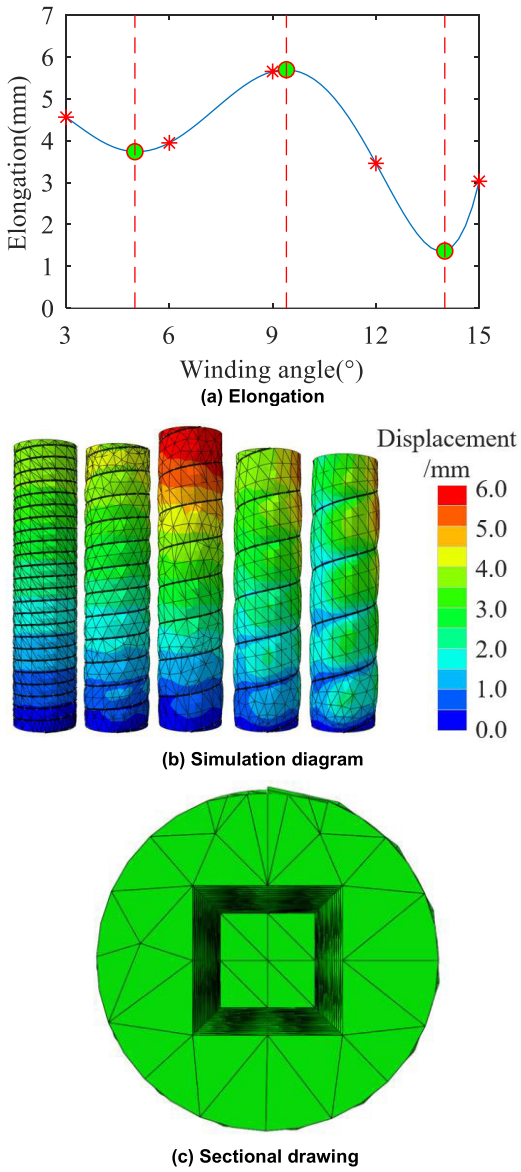

(a) Elongation

(b) Simulation diagram

(c) Sectional drawing

FIGURE 2. Square actuator.

leading to a reduction in axial elongation characteristics. When the winding angle increases from 5° to 9.4°, the elongation increases. Qualitative analysis suggests that as the constraint of the winding fibers on the soft channel decreases, the effect of axial elongation becomes more significant than circumferential expansion, resulting in an increase in axial elongation characteristics. When the winding angle increases from 9.4° to 14°, the elongation decreases. Qualitative analysis suggests that as the constraint of the winding fibers on the soft channel decreases, the effect of circumferential expansion becomes more significant than axial elongation, leading to a reduction in axial elongation characteristics. When the winding angle increases from 14° to 15°, the elongation increases. Qualitative analysis suggests that due to insufficient constraint of the winding fibers on the soft channel, the effect of circumferential expansion becomes more significant than axial elongation, resulting in poor axial elongation characteristics. The effect of circumferential expansion is greater than the axial elongation, and excellent characteristics of axial elongation cannot be obtained. the degree of circumferential expansion and axial elongation The maximum elongation value of 5.69 mm is achieved at a winding angle of approximately 9.4°. Therefore, when the actuator channel shape is square, a winding angle of around 9.4° is optimal.

C. REGULAR PENTAGONAL CHANNEL

The finite element analysis and regression analysis of the regular pentagonal channel actuator are shown in Fig. 3(a)-(c). Including the regression analysis of the elongation under different winding angles, the simulation results with Abaqus and the sectional drawing of regular pentagonal. The elongation values obtained from simulations and the time required for Abaqus simulations for the regular pentagonal channel actuator under specific winding angles are shown in Tab. 3.

TABLE 3. Elongation of regular pentagon channel actuators.

Angle of winding	3°	6°	9°	12°	15°
Elongation/mm	4.15	6.18	5.96	3.59	3.56
Time/s	291	96	52	106	84

The regression analysis, elongation, simulation results, and simulation time for the regular pentagonal channel actuator are shown in Fig. 3(a)-(b) and Tab. 3. As the winding angle increasing from 3° to 7.2°, the elongation increases. Through qualitative analysis, the actuator's characteristics of axial elongation is increases by the constraint of the winding fiber is gradually reduced on the soft channel. When the winding angle increases from 7.2° to 13.8°, the elongation decreases. Qualitative analysis suggests that as the constraint of the winding fibers on the soft channel decreases, the effect of circumferential expansion becomes more significant than axial elongation, leading to a reduction in axial elongation characteristics. When the winding angle increases from 13.8° to 15°, Qualitative analysis suggests that due to insufficient constraint of the winding fibers on the soft channel, the effect of circumferential expansion becomes more significant than axial elongation, resulting in poor axial elongation characteristics. The maximum elongation value of 6.41 mm is achieved at a winding angle of approximately 7.2°. Therefore, when the actuator channel shape is a regular pentagon, a winding angle of around 7.2° is optimal.

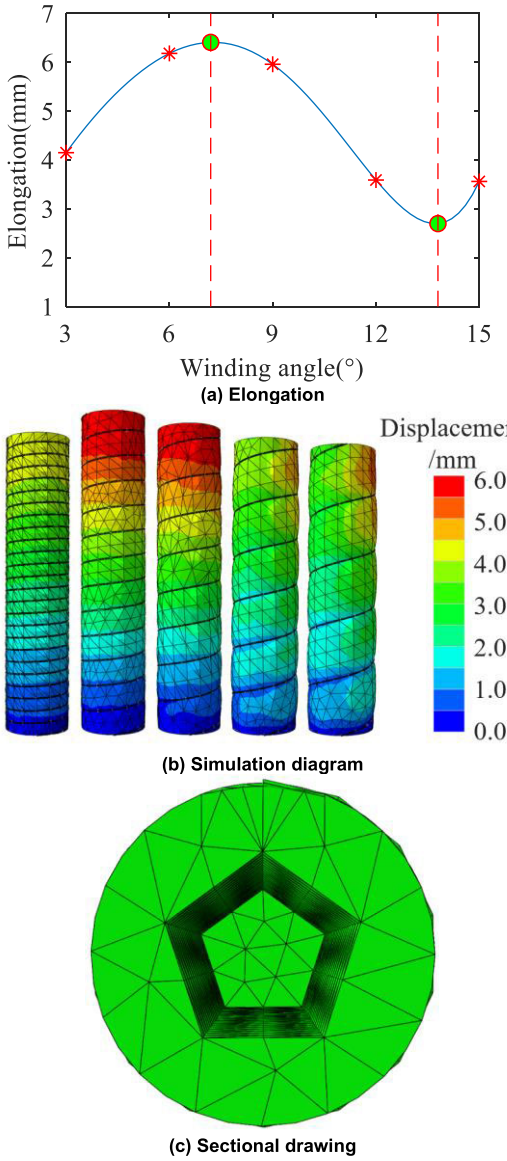

FIGURE 3. Regular pentagon actuator.

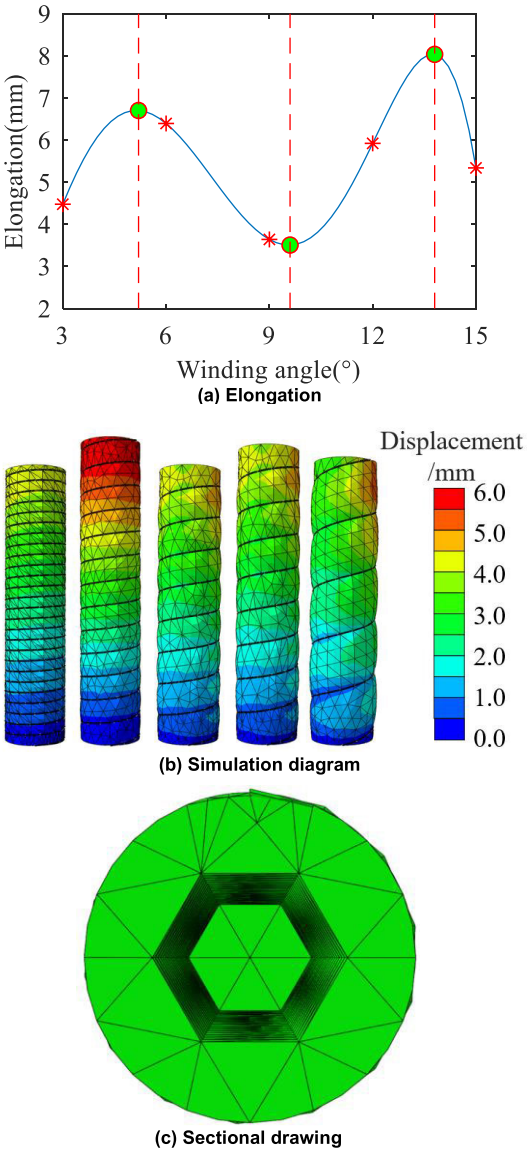

FIGURE 4. Regular hexagon actuator.

D. REGULAR PENTAGONAL CHANNEL

The finite element analysis and regression analysis of the regular hexagon channel actuator are shown in Fig. 4(a)-(c). Including the regression analysis of the elongation under different winding angles, the simulation results with Abaqus, and the sectional drawing of regular hexagon. The elongation values obtained from simulations and the time required for Abaqus simulations for the regular hexagon channel actuator under specific winding angles are shown in Tab. 4.

TABLE 4. Elongation of regular hexagon channel actuators.

Angle of winding	3°	6°	9°	12°	15°
Elongation/mm	4.48	6.39	3.64	5.92	5.34
Time/s	259	31	84	36	62

The regression analysis, elongation, simulation results, and simulation time for the regular hexagon channel actuators are shown in Fig. 4(a)-(b) and Tab. 4. As the winding angle increases from 3° to 5.2°, the elongation increases. Qualitative analysis suggests that as the constraint of the winding fibers on the soft channel decreases, leading to an increase in axial elongation characteristics. When the winding angle increases from 5.2° to 9.6°, the elongation decreases. Qualitative analysis suggests that as the constraint of the winding fibers on the soft channel decreases, the effect of axial elongation becomes more significant than circumferential expansion, resulting in an increase in axial elongation characteristics. When the winding angle increases from 9.6° to 13.8°, the elongation increases. Qualitative analysis suggests that as the constraint of the winding fibers on the soft channel decreases, the effect of axial elongation becomes

more significant than circumferential expansion, resulting in an increase in axial elongation characteristics. When the winding angle increases from 13.8° to 15°, the elongation decreases. Qualitative analysis suggests that as the constraint of the winding fibers on the soft channel decreases, the effect of circumferential expansion becomes more significant than axial elongation, leading to a reduction in axial elongation characteristics. The maximum elongation value of 5.69 mm is achieved at a winding angle of approximately 13.8°. Therefore, when the actuator channel shape is a regular hexagon, a winding angle of around 13.8° is optimal.

E. CIRCULAR CHANNEL

The finite element analysis and regression analysis of the circular channel actuator are shown in Fig. 5(a)-(c). Including the regression analysis of the elongation under different winding angles, the simulation results using Abaqus and the sectional drawing of circular. The elongation values obtained from simulations and the time required for Abaqus simulations for the circular channel actuator under specific winding angles are shown in Tab. 5.

TABLE 5. Elongation of circular channel rivers.

Angle of winding	3°	6°	9°	12°	15°
Elongation/mm	4.57	3.96	3.98	4.10	6.40
Time/s	257	62	82	68	197

The regression analysis, elongation, simulation results, and simulation time for the circular channel actuator are shown in Fig. 5(a)-(b) and Tab. 5. As the winding angle increases from 3° to 7.2°, the elongation decreases. Qualitative analysis suggests that as the constraint of the winding fibers on the soft channel decreases, the effect of circumferential expansion becomes more significant than circumferential elongation, resulting in a decrease in axial elongation characteristics. When the winding angle increases from 7.2° to 15°, the elongation increases. Qualitative analysis suggests that due to insufficient constraint of the winding fibers on the soft channel and the greater effect of axial elongation than circumferential expansion, the axial elongation characteristics improve. When the winding angle increases from 6° to 12°, the elongation of the circular actuator cannot change significantly with the increasing winding angle. The maximum elongation value of 6.41 mm is achieved at a winding angle of 15°. Therefore, when the soft channel shape of the actuator is circular, a winding angle of approximately 15° is optimal.

F. ANALYSIS OF DIFFERENT CHANNEL SHAPES

The reasons for the variation of the elongation of the actuators in A to E are qualitatively analyzed as follows. With the same section area and inflation length, the internal force of the elastic base is the same, and the gas pressure make the elastic base expand circumferentially and extend axially. According to the principle of conservation of energy and conservation of mass, the degree of circumferential expansion and axial

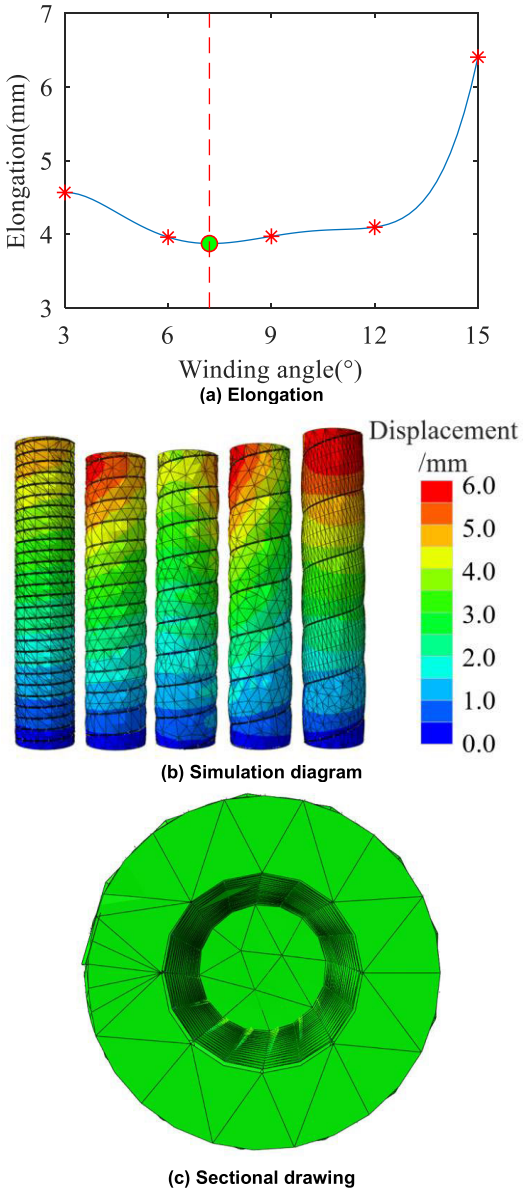

(a) Elongation

(b) Simulation diagram

(c) Sectional drawing

FIGURE 5. Circular actuator.

elongation is different under different winding angles. The purpose of this experiment is to find the optimal section shape and winding angle to maximize the elongation of the actuator. By comparing and analyzing the elongation of the soft actuator with different cross-sectional channel shapes, the total elongation sums at specific winding angles for various channel shapes, including equilateral triangle, square, regular pentagon, regular hexagon and circle, are shown in Tab. 6. The results of numerical simulation indicate that the hexagon has the longest total elongation. However, for the circular channel, as the winding angle increases to 15°, the elongation significantly increases while the circumferential expansion becomes more severe. By comprehensive comparison, circle and hexagon channel better than other cross-sectional shapes, the choice of cross-sectional shape can be made based on objective application requirements.

TABLE 6. Sum of elongation.

Section shape	Triangle	Quadri lateral	Pentag on	Hexag on	Circle
Elongation/mm	19.68	20.65	23.44	25.77	23.01

IV. NUMERICAL SIMULATION OF CIRCULAR CHANNEL ACTUATOR

A. NUMERICAL SIMULATION OF LENGTH

This section is focuses on the single-channel actuator with the pressure of 60 KPa, the wall thickness of 5mm, the fiber diameter of 0.5mm, and a winding angle of 9°. The simulation experiments are conducted with a step increment of 10 mm, ranging from 80 mm to 120 mm in soft channel length. According to the numerical simulation process introduced in Section II, the simulation results are as follows.

Fig. 6(a)-(b) shows the finite element analysis and regression analysis of the circular channel actuator at different soft channel lengths. It includes the regression analysis of the elongation of the circular channel actuator at different actuator lengths and the results of Abaqus simulation. At a specific soft channel length, the amount of elongation by simulation of the circular channel actuator and the time required for Abaqus simulation are shown in Tab. 7.

TABLE 7. Elongation of different soft length.

Length variation/mm	80	90	100	110	120
Elongation/mm	3.31	3.57	3.98	2.47	2.38
Time/s	149	80	82	33	32

The regression analysis, elongation, simulation results, and simulation time of the circular channel actuator are shown in Fig. 6(a)-(b) and Tab. 7. As the actuator length increases from 80mm to 83.2mm, the elongation decreases with the increasing soft channel length, indicating a decrease in elongation characteristics. When the length of the actuator increases from 83.2mm to 97.6mm, the elongation increases with the increasing actuator length, indicating an increase in elongation characteristics. As the actuator length increases from 97.6mm to 116mm, the elongation decreases with the increasing actuator length, resulting in a decrease in elongation characteristics. Finally, when the actuator length increases from 116mm to 120mm, the elongation increases with the increasing actuator length, indicating an increase in elongation characteristics. Therefore, the maximum elongation value of 4.04 mm is achieved when the soft channel length is 97.6 mm.

B. NUMERICAL SIMULATION ON WALL THICKNESS

This section is focuses on the single-channel actuator with the length of 100mm, the pressure of 60KPa, the fiber diameter of 0.5mm, and a winding angle of 9°. The simulation experiments are conducted with a step increment of 0.5 mm, ranging from 4 mm to 6 mm in wall thickness. the wall thickness incremental step is 0.5mm. According to the numerical simulation process in Section II, the simulation results are as follows.

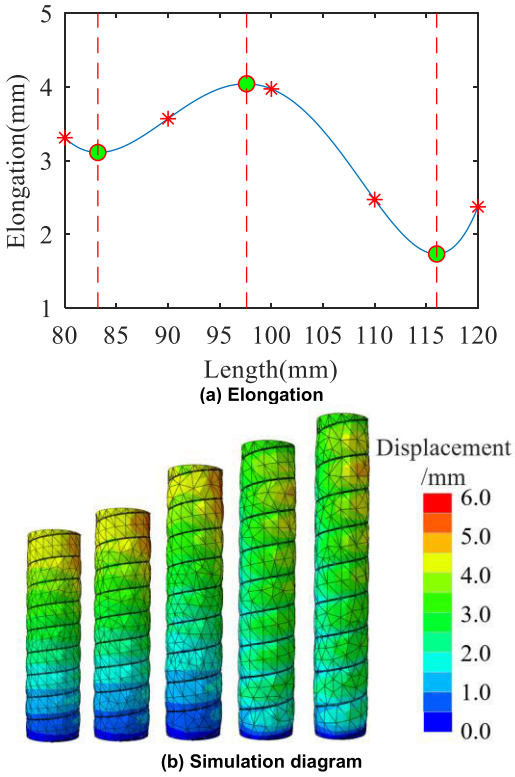

FIGURE 6. Different lengths of circular actuator.

Fig. 7(a)-(b) shows the finite element analysis and regression analysis of the circular channel actuator at different wall thicknesses. It includes the regression analysis of the elongation of the circular channel driver at different wall thickness and the results of Abaqus simulation. At specific wall thickness, the simulation elongation of circular channel actuator and the time required for Abaqus simulation are shown in Tab. 8.

TABLE 8. Elongation of circular actuators.

Wall thickness /mm	4	4.5	5	5.5	6
Elongation/mm	5.20	4.70	3.98	4.06	3.43
Time/s	76	192	82	44	95

The regression analysis, elongation, simulation results, and simulation time of circular channel actuator are shown in Fig. 7(a)-(b) and Tab. 8. As the wall thickness increases from 4mm to 4.08mm, the elongation increases with the increasing wall thickness, indicating an increase in elongation characteristics. When the wall thickness increases from 4.08mm to 5.16mm, the elongation decreases with the increasing wall thickness, resulting in a decrease in elongation characteristics. When the wall thickness increases from 5.16mm to 5.64mm, the elongation increases with the increasing wall thickness, indicating an increase in elongation characteristics.

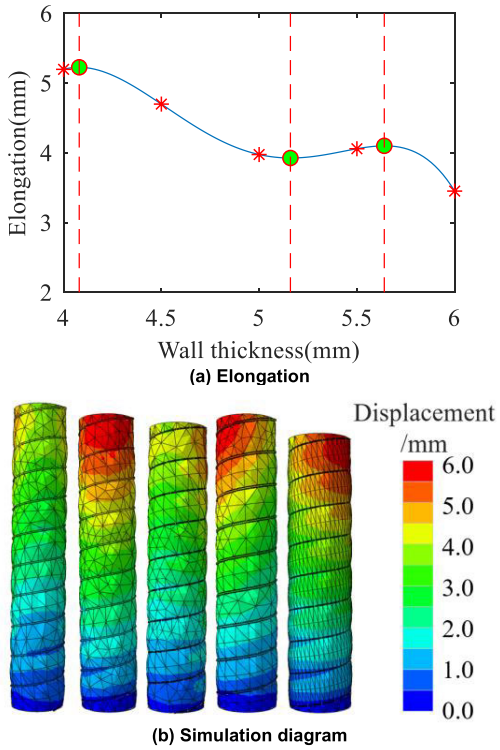

FIGURE 7. Different wall thicknesses of circular actuator.

Finally, When the wall thickness increases from 5.64mm to 6mm, the elongation decreases with the increase of wall thickness, the elongation characteristic decreases with the increasing wall thickness, resulting in a decrease in elongation characteristics. The maximum elongation value of 5.23 mm is achieved when the wall thickness is 4.08mm.

C. NUMERICAL SIMULATION OF THE DIAMETER OF FIBER

This section is focuses on the single-channel actuator with the length of 100mm, the pressure of 60KPa, the fiber diameter of 0.5mm, and a winding degree of 9°. The simulation experiments are conducted with a step increment of 0.1 mm, ranging from 0.3 mm to 0.7 mm in fiber diameter. According to the numerical simulation process introduced in Section II, the simulation results are as follows.

Fig. 8(a)-(b) are the finite element analysis and regression analysis of circular channel actuator at different fiber diameters. It includes the regression analysis of the elongation of the circular channel driver at different fiber diameters and the results of Abaqus simulation. At a specific winding fiber diameter, the simulation elongation of the circular channel actuator and the time required for the Abaqus simulation are shown in Tab. 9.

In particular, the actuator elongation is 5.264mm when the winding fiber diameter is 0.3mm. However, the wound fiber could not bear the pressure of 60KPa. There is no simulation time because the finite element calculation cannot converge and resulting in the actuator explosion.

The regression analysis, elongation, simulation results, and simulation time of circular channel actuator are shown in

TABLE 9. Elongation of fiber diameter.

Diameter of wound fiber /mm	0.3	0.4	0.5	0.6	0.7
Elongation/mm	5.26	4.27	3.98	4.06	4.09
Time/s	-	142	82	42	126

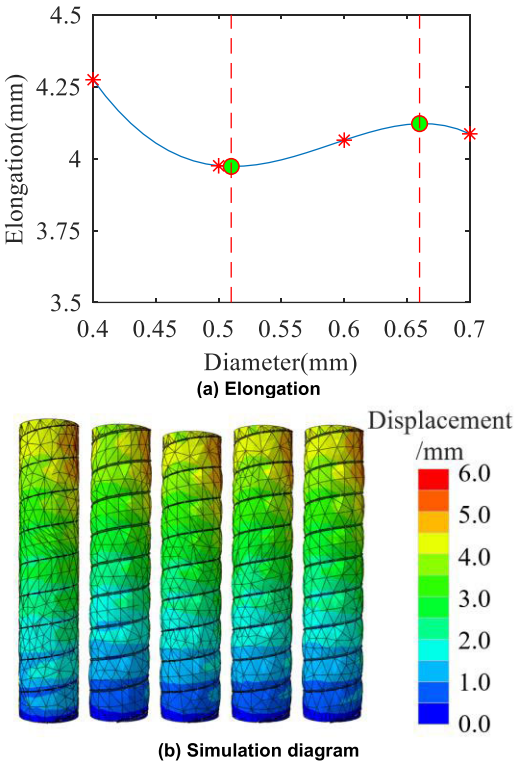

FIGURE 8. Different fiber diameter of circular actuator.

Fig. 8(a)-(b) and Tab. 9. As the fiber diameter increases from 0.4 to 0.51mm, the elongation decreases with the increasing fiber diameter, resulting in a decrease in elongation characteristics. When the fiber diameter increases from 0.51 to 0.66mm, the elongation increases with the increasing fiber diameter, indicating an increase in elongation characteristics. As the fiber diameter increases from 0.66 to 0.7mm, the elongation decreases with the increasing fiber diameter, resulting in a decrease in elongation characteristics. The maximum elongation value of 4.12 mm is achieved when the fiber diameter is 0.66 mm.

D. NUMERICAL SIMULATION OF THE MESH DENSITY

This section is focuses on the effect of mesh density with the length of 100mm, the pressure of 60KPa, the fiber diameter of 0.5mm, the fiber diameter of 0.5mm, and a winding degree of 9°. The simulation experiments are conducted with a step increment of 0.1 mm, ranging from 3 to 7 mm in mesh densities. According to the numerical simulation process introduced in Section II, the simulation results are as follows.

Fig. 9(a)-(b) are the finite element analysis and error percentage of circular channel actuator at different mesh

densities. It includes the error percentage of the elongation of the circular channel driver at different mesh densities and the results of Abaqus simulation. At a specific mesh density, the simulation elongation of the circular channel actuator, the time and error percentage for the Abaqus simulation are shown in Tab. 10.

TABLE 10. Elongation of mesh density.

Mesh density	3	4	5	6	7
Elongation/mm	4.10	4.04	3.98	3.93	3.99
Time/s	452	184	82	64	64
Percentage error	2.2%	0.9%	0.8%	1.9%	0.4%

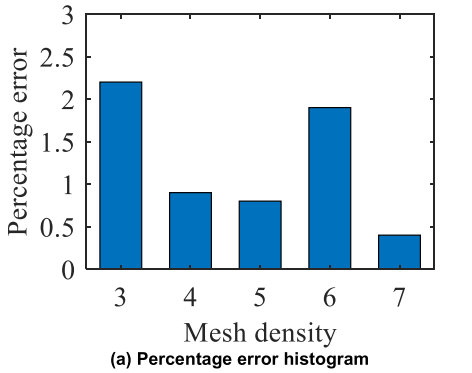

(a) Percentage error histogram

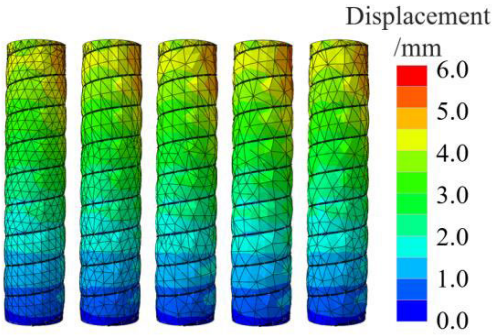

(b) Simulation diagram

FIGURE 9. Different mesh density of circular actuator.

The error percentage, elongation, simulation results, and simulation time of circular channel actuator are shown in Fig. 9(a)-(b) and Tab. 10. The mesh density is global seed which is the size of the unit on an entire part or entity. The average elongation of the circular actuator under different mesh densities is 4.01. The error percentage is the difference between the elongation and the average value divided by the average value. The maximum value of error percentage is 2.2%, which is very small and can be ignored. The accuracy of all simulations is proved by the mesh density simulation.

V. CONCLUSION

In this study, numerical simulation and regression analysis were conducted on the aerodynamic actuators with coupled fibers and soft channels. The experimental results on the cross-sectional shapes of soft channels indicate that the shape of the soft channel, such as equilateral triangle, square, pentagon, hexagon, and circle, has a significant impact on the performance of the soft actuator. Among them, the soft actuators with circular or hexagonal channels exhibit superior driving performance. The experimental results on the fiber winding diameter indicate that the circular soft actuator with a fiber diameter of 0.66 mm demonstrates better driving performance. However, the optimal winding angle of the soft actuator varies with the shape of the driving channel. The experimental results on the wall thickness and driving channel length show that the circular soft actuator with a wall thickness of 5.64 mm and a driving channel length of 97.6 mm exhibits superior driving performance. The aerodynamic actuators can be used in laparoscopic surgical robots and weightlessness in space due to their unique flexibility, accuracy and safety. Our future work will focus on fabricating single-channel soft actuators with optimal performance parameters based on the analysis of the individual channel units and designing multi-channel soft robots. This research provides an important theoretical basis for optimizing the parameters of soft actuators and soft robots, effectively improving the development efficiency of soft actuators and soft robots.

REFERENCES

[1] G. Y. Gu, J. Zhu, and L. M. Zhu, "A survey on dielectric elastomer actuators for soft robots," *Bioinspiration Biomimetics*, vol. 12, no. 1, pp. 3–11, Jan. 2022.

[2] C. H. Liu, L. J. Chen, J. C. Chi, and J. Y. Wu, "Topology optimization design and experiment of a soft pneumatic bending actuator for grasping applications," *IEEE Robot. Autom. Lett.*, vol. 7, no. 2, pp. 2086–2093, Apr. 2022.

[3] J. Frame, N. Lopez, O. Curet, and E. D. Engeberg, "Thrust force characterization of free-swimming soft robotic jellyfish," *Bioinspiration Biomimetics*, vol. 13, no. 6, Sep. 2018, Art. no. 064001.

[4] J. Cao, W. Liang, J. Zhu, and Q. Ren, "Control of a muscle-like soft actuator via a bioinspired approach," *Bioinspiration Biomimetics*, vol. 13, no. 6, Oct. 2018, Art. no. 066005.

[5] Z. Zhou, S. Kokubu, Y. Wang, Y. Lu, P. E. Tortós, and W. Yu, "Optimization of spring constant of a pneumatic artificial muscle-spring driven antagonistic structure," *IEEE Robot. Autom. Lett.*, vol. 7, no. 3, pp. 5982–5989, Jul. 2022.

[6] L. Yuanzhong, A. Takanishi, and H. Ishii, "Design of a soft rat robot based on pneumatic actuator," in *Proc. IEEE/ASME Int. Conf. Adv. Intell. Mechatronics (AIM)*, Jul. 2022, pp. 926–931.

[7] X. Lu, K. Wang, and T. Hu, "Development of an annelid-like peristaltic crawling soft robot using dielectric elastomer actuators," *Bioinspiration Biomimetics*, vol. 15, no. 4, Jun. 2020, Art. no. 046012.

[8] C. A. Daily-Diamond, A. Novelia, and O. M. O'Reilly, "Dynamical analysis and development of a biologically inspired SMA caterpillar robot," *Bioinspiration Biomimetics*, vol. 12, no. 5, Sep. 2017, Art. no. 056005.

[9] L. Wang and Z. Wang, "Mechanoreception for soft robots via intuitive body cues," *Soft Robot.*, vol. 7, no. 2, pp. 198–217, Apr. 2020.

[10] B. Li, H. Cao, B. Greenspan, and M. A. Lobo, "Development and evaluation of pneumatic actuators for pediatric upper extremity rehabilitation devices," *J. Textile Inst.*, vol. 113, no. 7, pp. 1372–1379, May 2021.

[11] K. Jung, J. C. Koo, J.-D. Nam, Y. K. Lee, and H. R. Choi, "Artificial annelid robot driven by soft actuators," *Bioinspiration Biomimetics*, vol. 2, no. 2, pp. 42–49, Jun. 2007.

[12] Q. Jiang and F. Xu, "Design and motion analysis of adjustable pneumatic soft manipulator for grasping objects," *IEEE Access*, vol. 8, pp. 191920–191929, 2020.

[13] B. Kaczmarski, D. E. Moulton, A. Goriely, and E. Kuhl, "Bayesian design optimization of biomimetic soft actuators," *Comput. Methods Appl. Mech. Eng.*, vol. 408, Apr. 2023, Art. no. 115939.

[14] M. S. Xavier, C. D. Tawk, A. Zolfagharian, J. Pinskier, D. Howard, T. Young, J. Lai, S. M. Harrison, Y. K. Yong, M. Bodaghi, and A. J. Fleming, "Soft pneumatic actuators: A review of design, fabrication, modeling, sensing, control and applications," *IEEE Access*, vol. 10, pp. 59442–59485, 2022.
[15] G. Singh, C. Xiao, E. T. Hsiao-Wecksler, and G. Krishnan, "Design and analysis of coiled fiber reinforced soft pneumatic actuator," *Bioinspiration Biomimetics*, vol. 13, no. 3, Apr. 2018, Art. no. 036010.
[16] C. Tawk, M. Panhuis, G. M. Spinks, and G. Alici, "Bioinspired 3D printable soft vacuum actuators for locomotion robots, grippers and artificial muscles," *Soft Robot.*, vol. 5, no. 6, pp. 685–694, Dec. 2018.
[17] B. Mazzolai, L. Margheri, M. Cianchetti, P. Dario, and C. Laschi, "Soft-robotic arm inspired by the octopus: II. From artificial requirements to innovative technological solutions," *Bioinspiration Biomimetics*, vol. 7, no. 2, May 2012, Art. no. 025005.
[18] M. Li, A. Pal, A. Aghakhani, A. Pena-Francesch, and M. Sitti, "Soft actuators for real-world applications," *Nature Rev. Mater.*, vol. 7, no. 3, pp. 235–249, Nov. 2021.
[19] L. Chen, W. Chen, Y. Xue, J.-W. Wong, Y. Liang, M. Zhang, X. Chen, X. Cao, Z. Zhang, and T. Li, "An untethered soft chemo-mechanical robot with composite structure and optimized control," *Extreme Mech. Lett.*, vol. 27, pp. 27–33, Feb. 2019.
[20] J. Li, L. Liu, Y. Liu, and J. Leng, "Dielectric elastomer spring-roll bending actuators: Applications in soft robotics and design," *Soft Robot.*, vol. 6, no. 1, pp. 69–81, Feb. 2019.
[21] E. Natarajan, K. Y. Chia, and A. M. Faudzi, "Bio inspired salamander robot with Pneu-Net soft actuators-design and walking gait analysis," *Bull. Polish Acad. Sci., Tech. Sci.*, vol. 69, no. 3, pp. 1–11, May 2021.
[22] W. Wang, Y. Zhu, S. Cai, and G. Bao, "Ultralong stretchable soft actuator (US2A): Design, modeling and application," *Chin. J. Mech. Eng.*, vol. 36, no. 1, pp. 1–12, Feb. 2023.
[23] M. Liu, Z. Xu, J. J. Ong, J. Zhu, and W. F. Lu, "An earthworm-like soft robot with integration of single pneumatic actuator and cellular structures for peristaltic motion," in *Proc. IEEE/RSJ Int. Conf. Intell. Robots Syst. (IROS)*, Oct. 2020, pp. 7840–7845.
[24] E. A. Allen and J. P. Swensen, "Design of a highly-maneuverable pneumatic soft actuator driven by intrinsic SMA coils (PneuSMA actuator)," in *Proc. IEEE/RSJ Int. Conf. Intell. Robots Syst. (IROS)*, Oct. 2020, pp. 8667–8672.
[25] T. Kanno, S. Ohkura, O. Azami, T. Miyazaki, T. Kawase, and K. Kawashima, "Model of a coil-reinforced cylindrical soft actuator," *Appl. Sci.*, vol. 9, no. 10, p. 2109, May 2019.
[26] R. G. Treloar, "The elasticity of a network of long-chain molecules," *Trans. Faraday Soc.*, vol. 39, no. 1, pp. 36–41, 1943.
[27] S. D. Barforooshi and A. K. Mohammadi, "Study neo-Hookean and Yeoh hyper-elastic models in dielectric elastomer-based micro-beam resonators," *Latin Amer. J. Solids Struct.*, vol. 13, no. 10, pp. 1823–1837, Oct. 2016.
[28] B. Wang, Q. Lyu, L. Jiang, Y. Chen, and Z. Guo, "An extended Hertz model for incompressible Mooney–Rivlin half-space under finite spherical indentation," *Int. J. Appl. Mech.*, vol. 14, no. 10, pp. 1–13, Jan. 2023.
[29] O. H. Yeoh, "Characterization of elastic properties of carbon-black-filled rubber vulcanizates," *Rubber Chem. Technol.*, vol. 63, no. 5, pp. 792–805, Nov. 1990.
[30] O. H. Yeoh, "Some forms of the strain energy function for rubber," *Rubber Chem. Technol.*, vol. 66, no. 5, pp. 754–771, Nov. 1993.
[31] J. D. van Tonder, M. P. Venter, and G. Venter, "A novel method for resolving non-unique solutions observed in fitting parameters to the Mooney Rivlin material model," *Finite Elements Anal. Design*, vol. 225, Nov. 2023, Art. no. 104006.
[32] H. Bechir, F. Mendil, and K. Yaya, "Extension and inflation of a thick-cylindrical tube made of isotropic compressible of Mooney–Rivlin materials: Modeling and finite element simulations," *Acta Mechanica*, vol. 1, pp. 1–15, Aug. 2023.
[33] M. Destrade and G. Saccomandi, "Plane-polarised finite-amplitude shear waves in deformed incompressible materials," *Math. Mech. Solids*, vol. 27, no. 8, pp. 1494–1503, Apr. 2022.
[34] W. B. Niu, Y. M. Li, Y. H. Ma, and G. F. Zhao, "Determination and prediction of time-varying parameters of Mooney–Rivlin model of rubber material used in natural rubber bearing under alternating of aging and seawater erosion," *Materials*, vol. 16, no. 13, p. 4696, Jun. 2023.
[35] I. J. Sánchez-Arce, D. C. Gonçalves, L. D. C. Ramalho, R. D. S. G. Campilho, and J. Belinha, "The Ogden model and the natural neighbour radial point interpolation method for hyperelastic analyses," *J. Brazilian Soc. Mech. Sci. Eng.*, vol. 45, no. 1, pp. 1–10, Jan. 2023.
[36] M. Lengger, G. Possart, and P. Steinmann, "A viscoelastic Mooney–Rivlin model for adhesive curing and first steps toward its calibration based on photoelasticity measurements," *Arch. Appl. Mech.*, vol. 92, no. 12, pp. 3943–3965, Dec. 2022.
[37] P. Polygerinos, Z. Wang, J. T. B. Overvelde, K. C. Galloway, R. J. Wood, K. Bertoldi, and C. J. Walsh, "Modeling of soft fiber-reinforced bending actuators," *IEEE Trans. Robot.*, vol. 31, no. 3, pp. 778–789, Jun. 2015.
[38] Z. Zhang, X. Wang, H. Liu, B. Liang, and S. Wang, "Kinematic analysis of novel soft robotic arm based on virtual work principle," in *Proc. IEEE Int. Conf. Robot. Biomimetics (ROBIO)*, Dec. 2018, pp. 984–990.
[39] Z. Zhang, X. Wang, S. Wang, D. Meng, and B. Liang, "Design and modeling of a parallel-pipe-crawling pneumatic soft robot," *IEEE Access*, vol. 7, pp. 134301–134317, 2019.

WANG SONGTAO (Member, IEEE) received the B.S., M.S., and Ph.D. degrees in mechanical engineering from the China University of Mining and Technology, Xuzhou, China, in 2010, 2013, and 2017, respectively.

He is currently an Associate Professor with the Department of Mechanical Engineering, Nanchang Institute of Technology. His research interests include intelligence robotics, continuum robotics, dynamic modeling, and control.

YU YIMENG received the B.S. degree in mechanical and electrical engineering from the Nanchang Institute of Technology, Nanchang, China, in 2022, where he is currently pursuing the M.S. degree in electronic and information engineering.

His research interests include the design, modeling, and control of pneumatic soft robots.

JIANG SHIYU received the B.S. degree in computer science and technology from the Jingdezhen Ceramic Institute, in 2014, the M.S. degree in statistics from Jingdezhen Ceramic University, in 2017, and the Ph.D. degree in materials processing engineering from Nanchang University, in 2021.

She is currently a Lecturer in mechanical engineering with the Nanchang Institute of Technology. Her research interests include polymer processing technology, mechanical design and manufacturing, and processing and manufacturing of soft robot bodies.

CHEN SISI received the B.S. degree in mechanical engineering from the Nanchang Institute of Technology, Nanchang, China, in 2022, where she is currently pursuing the M.S. degree in electronic and information engineering.

Her research interests include the design, modeling, and control of pneumatic soft robots.